Small-Signal Modeling and Comparisons of the Pulse Frequency Modulation and Time Shift Control for the *LLC* Converters

Zhiqiang Guo, *Senior Member, IEEE*, Zhijie Huang, and Zhongyuan Chen

***Abstract*—This article describes a new method for the small-signal modeling of the *LLC* converter based on time-domain analysis. The time-domain expressions of the state trajectory are transformed to the first-order of Tylor's expressions, which can achieve the linearization of the trajectory expressions. The state space formulas and transfer functions in pulse frequency modulation (PFM) are derived from the linearization expressions, where the state variables include the initial resonant current and resonant capacitor voltage in a switching period besides the output voltage. This method can be easily extended to the small signal modeling of the *LLC* converter in time-shift control (TSC). The reason why the TSC is regarded as a current-mode control is analytically explained in this article. The comparison of the frequency response in the PFM and TSC demonstrates the high bandwidth and high phase margin in the TSC, which indicates the *LLC* converter with the TSC can achieve a good dynamic response. The closed-loop PI controller is designed based on the small-signal model, and load step experiments demonstrate that the converter exhibits better dynamic response in the TSC compared to the PFM.**

***Index Terms*—*LLC* converter, pulse frequency modulation (PFM), small-signal analysis, time-domain analysis, time-shift control (TSC).**

I. Introduction

THE *LLC* resonant converter can operate in both boost and buck modes while maintaining zero voltage switching (ZVS), ensuring a wide voltage regulation range and high efficiency. As a result, it has been widely used in data centers, electric vehicles, fuel cells, and industrial power supplies [1], [2], [3]. Therefore, it is crucial to research the control strategies and modeling methods for *LLC* converters to achieve better frequency response.

The typical control strategy of the *LLC* converter is pulse frequency modulation (PFM), in which the output-voltage loop directly regulates the switching frequency [4]. However, the single voltage mode control cannot guarantee a superior dynamic response [5]. One kind of method to improve the dynamic response is to improve the structure of the controller. An adaptive voltage-controlled oscillator (VCO) can adjust the low-frequency magnitude in frequency response to improve the dynamic performance of the *LLC* converter [6]. The other kind of method to improve the dynamic response is to apply the current mode control [7]. Because of the approximate sinusoidal resonant inductor current, it cannot be used as the inner current feedback. In [8], an average resonant current obtained by a rectifier circuit is introduced as the feedback of the inner current loop. The rectifier circuit filters out the high-frequency components, and it also limits the performance of the current mode control. Onsemi provides an analog integrated circuit FAN7688 to achieve the charged control for good dynamic response in *LLC* converters [9]. The feedback of the current loop is the integration of the resonant current in half of a switching period. Apart from the resonant inductor current, the resonant capacitor voltage is also an indicator of energy stored in the resonant tank. Therefore, the capacitor voltage at the instant when switching is taking place is set as the feedback of the inner current loop in the charged control, which demonstrates the good frequency response [10]. A bang-bang control triggers the switching action by the resonant capacitor voltage level for the fast dynamic response [11], and it is also regarded as a current mode control. Based on the bang-bang control in [11], an analog integrated circuit UCC256302 is manufactured by Texas Instruments [12]. The charged control and bang-bang control are difficult to implement in digital controllers. A time-shift control (TSC) is another current mode control for *LLC* converters proposed by STMicroelectronics and it is proved that the TSC has better frequency response by simulation [13]. The zero-crossing detection of the resonant current is necessary in the TSC, which can be achieved by the analog circuit STNRG011 provided by STMicroelectronics [14]. Moreover, the TSC is easy to implement in digital controllers for *LLC* resonant converters [15].

To analyze the bandwidth and stability of the control loop for the *LLC* resonant converter, the frequency response based

Received 23 January 2024; revised 27 May 2024 and 15 August 2024; accepted 14 September 2024. Date of publication 18 September 2024; date of current version 12 December 2024. This work was supported in part by the National Natural Science Foundation of China under Grant 52477174 and in part by Beijing Natural Science Foundation under Grant 3232052. Recommended for publication by Associate Editor M. Ordonez. *(Corresponding authors: Zhiqiang Guo; Zhongyuan Chen.)*

Zhiqiang Guo and Zhijie Huang are with the School of Automation, Beijing Institute of Technology, Beijing 100081, China, and also with the Tangshan Research Institute, Beijing Institute of Technology, Tangshan 063099, China (e-mail: guozq32@bit.edu.cn; 3120220839@bit.edu.cn).

Zhongyuan Chen is with the Beijing Institute of Smart Energy, Beijing 102200, China (e-mail: chenzhongyuan@bise.hrl.ac.cn).

The detailed derivation of the small signal modeling and the MATLAB code for the modeling can be accessed at https://github.com/Guozq32/LLC-small-signal-modeling.

Color versions of one or more figures in this article are available at https://doi.org/10.1109/TPEL.2024.3463956.

Digital Object Identifier 10.1109/TPEL.2024.3463956

on the small-signal model must be evaluated. Different from the pulsewidth modulation controlled dc–dc converters, the small-signal modeling of the resonant converter is difficult to derive from the state-space averaged method [16]. Therefore, the fundamental harmonic analysis (FHA) and extended describing function (EDF) are applied to the resonant converter [17], [18]. On this basis, the small-signal modeling of the *LLC* converter is developed in [19] and [20]. To simplify the model, an equivalent circuit of the *LLC* also can be derived from the EDF [21]. This method can present an accurate frequency response when the switching frequency is close to the resonant frequency. However, when the switching frequency deviates from the resonant frequency, the small-signal modeling based on the EDF is imprecise. In [22], the synchronous reference frame (SRF) based modeling approach is developed, which takes the parasitic parameters of the *LLC* converter into account. However, it lacks the comparison between experimental results and the theoretical model to verify the accuracy of the model. A small-signal modeling method based on communication theory is proposed in [23], which reveals that the higher order harmonics and sideband frequencies have significant contributions in the small signal modeling, but its model exhibits low accuracy. To improve the accuracy of the small-signal modeling of the *LLC* in a wide switching frequency range, the harmonics components extracted by the Fourier transformation are taken into account [24]. Although the model agrees well with the real *LLC* converter, the derivation and expression of the model are too complicated to guide the controller design for the engineers. To overcome the inaccuracy of the FHA for the *LLC* converter, the time-domain analysis is proposed in [25] and [26] to obtain the gain of the converter and the working modes. On this basis, a discrete-time small-signal modeling method is applied to the *LLC* converter [27]. The VCO is frequency-dependent rather than a constant gain. In [27], the small-signal model considering the nonlinearity of the voltage-controlled oscillator is deduced, and it can achieve high accuracy in a wide range of switching frequency. The dynamic performance of *LLC* in the time domain is analyzed in [28], and the approach to derive the small-signal model is briefly introduced without providing a detailed derivation process.

Although the current mode control for the *LLC* converter can achieve better dynamic response, the small-signal modeling in current mode control is much more complicated than the voltage mode control in PFM. The above small-signal modeling methods all focus on the transfer function from switching frequency to output voltage in PFM, which are difficult to extend to the current mode control. Most of the frequency response of the current mode control for the *LLC* converter is based on simulation, and few articles present an accurate small-signal modeling of the current mode control. Furthermore, no article explains how to do the modeling of the TSC.

In this article, the time-domain expressions of the *LLC* converter are obtained based on planar trajectories. An accurate small-signal modeling for PFC is derived in the time domain using linearization at a steady-state operating point, demonstrating high accuracy over a wide range of switching frequencies. By establishing the relationship between the control time of TSC and the switching period, this method can easily extend the small-signal modeling of PFM to the small-signal modeling of TSC, which is also the contribution of this article. The analysis of the modeling reveals that TSC is a reduced-order model with better frequency response.

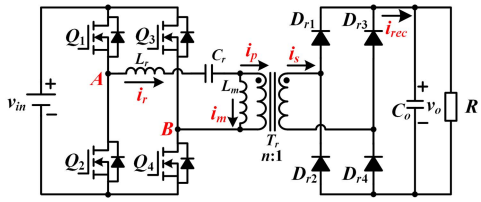

Fig. 1. Topology of the *LLC* resonant converter.

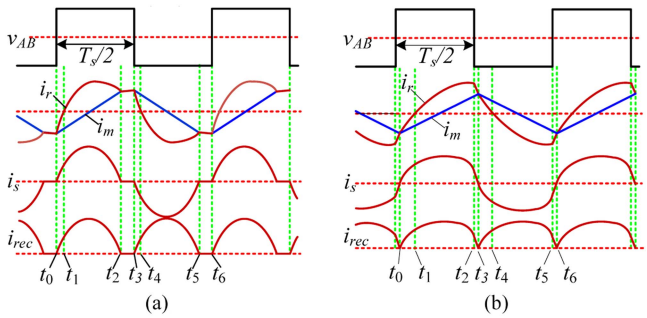

Fig. 2. Typical waveforms of the *LLC* resonant converter. (a) $f_s < f_r$. (b) $f_s > f_r$.

The rest of this article is organized as follows. Section II reviews the working modes of the *LLC* converter and gives the expressions of the state trajectory in the time domain. The calculation procedure of the steady-state operating point is presented. Section III gives the small-signal modeling of the *LLC* converter in PFM by using first-order Tylor expansions. Section IV presents the small-signal modeling of the *LLC* converter in TSC, and the reason why the TSC can be regarded as the current mode control is first analytically revealed. The comparisons of the PFM and TSC in frequency response are analyzed. In Section V, the bode diagrams tested in the experiments and the load step experiments verify the good frequency response in TSC. Finally, Section VI concludes this article.

II. Review of the Working Mode of the *LLC* Converter

A. LLC *Converter in Time-Domain Analysis*

The topology of the full-bridge *LLC* resonant converter is shown in Fig. 1, where $v_{\rm in}$ and v_o represent the input and output voltages. C_o denotes the output capacitor, and R is the load resistance. The primary stage is composed of Q_1-Q_4, and the rectifier stage is composed of D_{r1}-D_{r4}. The resonant tank consists of resonant inductor L_r, resonant capacitor C_r, and magnetizing inductor L_m of the transformer. It operates in three resonant stages based on the voltage v_m across the magnetizing inductor: positive clamped stage $v_m = nv_o$ (State P), negative clamped stage $v_m = -nv_o$ (Stage N), and the freewheeling stage $|v_m| < nv_o$ (State O). For the ZVS of the switches, the *LLC*

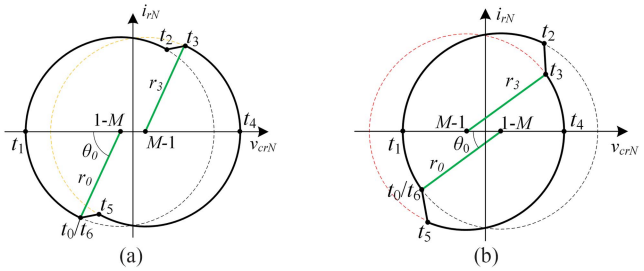

Fig. 3. Planar trajectories of the *LLC* resonant converter. (a) PO mode for $f_s < f_r$. (b) NP mode for $f_s > f_r$.

converter is suggested to work in PO mode for $f_s < f_r$ and NP mode for $f_s > f_r$ [25]. Therefore, the PO mode and NP mode will be analyzed below. The other modes can be analyzed in the same method. In Fig. 2(a), key waveforms are illustrated for $f_s < f_r$, where f_s is the switching frequency and the resonant frequency f_r is $1/(2\pi\sqrt{L_r C_r})$. Fig. 2(b) displays key waveforms for $f_s > f_r$.

To facilitate the subsequent theoretical analysis, the time when the resonant current is equal to the magnetizing current is selected as t_0. The voltage across the resonant tank is v_{AB}. i_r and i_m represent the resonant current and magnetizing current. The transformer secondary current i_s is rectified to $i_{\rm rec}$.

The state trajectory of the *LLC* resonant converter is introduced in [29] to analyze the operating modes and can be used to calculate the steady-state operating point. To simplify the analysis of the quiescent operating points, it is assumed that the output capacitor C_o is so large that the output voltage is approximately constant. In addition, the circuit losses and the dead time of Q_1-Q_4 are negligible.

The planar trajectories of the *LLC* resonant converter are shown in Fig. 3. Variables with the subscript *N* are normalized in this article, where voltages are normalized with the voltage factor $v_{\rm in}$ and currents are normalized with the current factor $I_N = v_{in}/Z_0$. Z_0 is the characteristic impedance, expressed as $\sqrt{L_r/C_r}$, and the voltage gain M is defined as $M = nv_o/v_{\rm in}$.

1) $f_s < f_r$ [see Fig. 2(a)]: From t_0 to t_2, the converter operates in P mode, and the magnetizing inductor L_m is clamped by the output voltage. The energy is transmitted from the input to the load. The trajectory behaves as a circle with the center (1-M, 0). r_0 is the radius of the trajectory, and θ_0 is the initial phase. Both are influenced by M, the resonant current i_{r0N}, and resonant capacitor voltage v_{cr0N} at t_0, as shown in (1) and (2). In this article, the normalized resonant current and resonant capacitor voltage at the time of t_k are denoted as i_{rkN} and v_{crkN}

$$r_0 = \sqrt{{i_{r0N}}^2 + [v_{cr0N} - (1-M)]^2} \tag{1}$$

$$\theta_0 = \arctan\left(-\frac{i_{r0N}}{v_{cr0N} - (1-M)}\right). \tag{2}$$

i_{r2N} and v_{cr2N} can be expressed as (3). φ_0 represents the angle of the trajectory from t_0 to t_2, and it can be calculated by $\omega_{r0}(t_2\text{-}t_0)$. ω_{r0} is defined as $1/\sqrt{L_r C_r}$

$$\begin{cases} i_{r2N} = r_0 \sin(\varphi_0 + \theta_0) \\ v_{cr2N} = -r_0 \cos(\varphi_0 + \theta_0) + (1-M) \end{cases}. \tag{3}$$

From t_2 to t_3, the converter operates in O mode. L_r, C_r, and L_m are involved in resonance. There is no energy transmitted to the output, and i_{mN} is equal to i_{rN}. The trajectory of this stage is part of an ellipse with center (1, 0), r_1 and θ_1 is determined by i_{r2N} and v_{cr2N}, as shown in (4) and (5), where $L_n = L_m/L_r$

$$r_1 = \sqrt{(1+L_n)\,{i_{r2N}}^2 + (v_{cr2N} - 1)^2} \tag{4}$$

$$\theta_1 = \arctan\left(-\frac{\sqrt{1+L_n}\, i_{r2N}}{v_{cr2N} - 1}\right). \tag{5}$$

In this mode, i_{r3N} and v_{cr3N} at t_3 can be expressed in (6), where φ_1 is the angle of the trajectory and can be calculated by $\omega_{r1}(t_3\text{-}t_2)$. ω_{r1} is defined as $1/\sqrt{(L_r + L_m)C_r}$

$$\begin{cases} v_{cr3N} = -r_1 \cos(\varphi_1 + \theta_1) + 1 \\ i_{r3N} = \frac{r_1}{\sqrt{1+L_n}} \sin(\varphi_1 + \theta_1) \end{cases}. \tag{6}$$

Because of the semiperiod symmetry, the trajectory from t_0 to t_3 is symmetric with the trajectory from t_3 to t_6, which will not be discussed in detail.

2) $f_s > f_r$ [see Fig. 2(b)]: When $f_s > f_r$, only L_r and C_r are involved in the resonance during the entire switching cycle. From t_0 to t_2, the trajectory is the same as $f_s < f_r$. From t_2 to t_3, the converter operates in N mode. The voltage across the resonant tank is changed to -$v_{\rm in}$, and the trajectory behaves as a circle with the center (-1-M, 0). r_1 is the radius of the trajectory and θ_1 is the initial phase in this mode. They can be calculated as

$$r_1 = \sqrt{{i_{r2N}}^2 + [v_{cr2N} + (1+M)]^2} \tag{7}$$

$$\theta_1 = \pi + \arctan\left(-\frac{i_{r2N}}{v_{cr2N} + 1 + M}\right). \tag{8}$$

i_{r3N} and v_{cr3N} can be expressed in (9), where $\varphi_1 = \omega_{r0}(t_3\text{-}t_2)$. The state trajectory from t_3 to t_6 can be obtained using a similar method and will not be discussed in detail

$$\begin{cases} i_{r3N} = r_1 \sin(\varphi_1 + \theta_1) \\ v_{cr3N} = -r_1 \cos(\varphi_1 + \theta_1) - (1+M) \end{cases}. \tag{9}$$

The time-domain expressions of i_{rN} and v_{crN} in different modes for $f_s < f_r$ and $f_s > f_r$ are given in Table I, and the definitions of r_k, θ_k, φ_k are similar to the previous analysis in the following discussion.

B. Calculation of the Steady-state Operation Point

1) $f_s < f_r$: For $f_s < f_r$, the normalized magnetizing current i_{mN} can be expressed as (10) from t_0 to t_2, and the normalized current i_{sN} flowing through the secondary side of the transformer is shown in (11). The average current $\bar{i}_{s1}$ on the secondary side from t_0 to t_3 is expressed as (12), and the output voltage $V_{\rm o}$ can be expressed as $R\bar{i}_{\rm rec}$, where the average rectified current $\bar{i}_{rec}$ is equal to $\bar{i}_{s1}$ from t_0 to t_3 in the steady state

$$i_{mN} = r_0 \sin(\theta_0) + \frac{M}{L_n}\omega_{r0}(t - t_0) \tag{10}$$

TABLE I
TIME-DOMAIN EXPRESSIONS OF i_{rN} AND v_{crN} IN DIFFERENT MODES

f_s \ t	t_0-t_2	t_2-t_3	t_3-t_5	t_5-t_6
$f_s < f_r$	$i_{rN} = r_0 \sin\left[\omega_{r0}(t-t_0)+\theta_0\right]$ $v_{crN} = -r_0 \cos\left(\omega_{r0}(t-t_0)+\theta_0\right)$ $+(1-M)$	$i_{rN} = \frac{r_1}{\sqrt{1+L_n}} \sin\left[\omega_{r1}(t-t_2)+\theta_1\right]$ $v_{crN} = -r_1 \cos\left[\omega_{r1}(t-t_2)+\theta_1\right]+1$	$i_{rN} = r_2 \sin\left[\omega_{r0}(t-t_3)+\theta_2\right]$ $v_{crN} = -r_2 \cos\left[\omega_{r0}(t-t_3)+\theta_2\right]$ $-(1-M)$	$i_{rN} = \frac{r_3}{\sqrt{1+L_n}} \sin\left[\omega_{r1}(t-t_5)+\theta_3\right]$ $v_{crN} = -r_3 \cos\left[\omega_{r1}(t-t_5)+\theta_3\right]-1$
$f_s > f_r$	$i_{rN} = r_0 \sin\left[\omega_{r0}(t-t_0)+\theta_0\right]$ $v_{crN} = -r_0 \cos\left[\omega_{r0}(t-t_0)+\theta_0\right]$ $+(1-M)$	$i_{rN} = r_1 \sin\left[\omega_{r0}(t-t_2)+\theta_1\right]$ $v_{crN} = -r_1 \cos\left[\omega_{r0}(t-t_2)+\theta_1\right]$ $-(1+M)$	$i_{rN} = r_2 \sin\left[\omega_{r0}(t-t_3)+\theta_2\right]$ $v_{crN} = -r_2 \cos\left[\omega_{r0}(t-t_3)+\theta_2\right]$ $-(1-M)$	$i_{rN} = r_3 \sin\left[\omega_{r0}(t-t_5)+\theta_3\right]$ $v_{crN} = -r_3 \cos\left[\omega_{r0}(t-t_5)+\theta_3\right]$ $+(1+M)$

$$i_{sN} = n\left(i_{rN} - i_{mN}\right) \tag{11}$$

$$\bar{i}_{s1} = \frac{2nI_n}{\omega_{r0}t_s}\left[r_0\cos(\theta_0) - r_0\cos(\varphi_0+\theta_0) - r_0\sin(\theta_0)\varphi_0 - \frac{M}{2L_n}{\varphi_0}^2\right]. \tag{12}$$

Because of the semi-period symmetry, the i_{r0N} and v_{cr0N} at t_0 are equal to the negative of i_{r3N} and v_{cr3N} respectively. Mode P transitions to Mode O at t_2, with the resonant current i_{rN} equal to the magnetizing current i_{mN}. Along with the definitions of M, φ_0, and φ_1, the equations can be expressed as

$$\begin{cases} r_0\sin(\varphi_0+\theta_0) - \frac{r_1}{\sqrt{1+L_n}}\sin(\theta_1) = 0 \\ -r_0\cos(\varphi_0+\theta_0) - M + r_1\cos(\theta_1) = 0 \\ \frac{r_1}{\sqrt{1+L_n}}\sin(\varphi_1+\theta_1) + r_0\sin(\theta_0) = 0 \\ -r_1\cos(\varphi_1+\theta_1) - r_0\cos(\theta_0) + (2-M) = 0 \\ r_0\sin(\varphi_0+\theta_0) - r_0\sin(\theta_0) - \frac{M}{L_n}\varphi_0 = 0 \\ M - \frac{2n^2RI_n}{T_sV_{in}\omega_{r0}}[r_0\cos(\theta_0) - r_0\cos(\varphi_0+\theta_0) \\ -r_0\sin(\theta_0)\varphi_0 - \frac{M}{2L_n}{\varphi_0}^2] = 0 \\ \frac{\varphi_0}{\omega_{r0}} + \frac{\varphi_1}{\omega_{r1}} - \frac{T_s}{2} = 0 \end{cases}. \tag{13}$$

$[r_0 \quad \theta_0 \quad \varphi_0 \quad r_1 \quad \theta_1 \quad \varphi_1 \quad M]$ is defined as the variables to be solved under the steady state. By using the Newton–Raphson iteration method, the solution of the equations can be calculated, so the steady-state operating point of the system will be obtained.

2) $f_s > f_r$: For $f_s > f_r$, the expression of i_{mN} is the same as (10) from t_0 to t_3. The current i_{sN} on the secondary side and the average current $\bar{i}_{s1}$ from t_0 to t_3 can be expressed as (11) and (14). By using a similar method for $f_s < f_r$, equations for $f_s > f_r$ can be deduced as (15). Solving (15) by the Newton–Raphson iteration method, the steady-state operating point for $f_s > f_r$ can be also obtained

$$\bar{i}_{s1} = \frac{2nI_n}{T_s\omega_{r0}}[r_0\cos(\theta_0) - r_0\cos(\varphi_0+\theta_0) + r_1\cos(\theta_1) - r_1\cos(\varphi_1+\theta_1)] \tag{14}$$

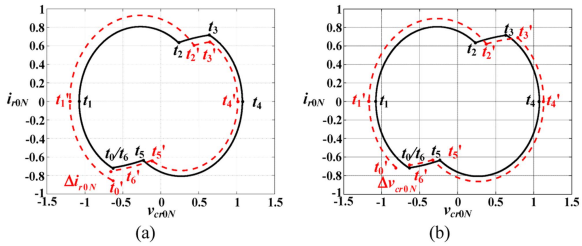

Fig. 4. Trajectories of the *LLC* converter for $f_s < f_r$. (a) i_{r0N} is disturbed. (b) v_{cr0N} is disturbed.

$$\begin{cases} r_0\sin(\theta_0) + \frac{M\omega_{r0}T_s}{4L_n} = 0 \\ r_0\sin(\varphi_0+\theta_0) - r_1\sin(\theta_1) = 0 \\ -r_0\cos(\varphi_0+\theta_0) + r_1\cos(\theta_1) + 2 = 0 \\ r_1\sin(\varphi_1+\theta_1) + r_0\sin(\theta_0) = 0 \\ -r_1\cos(\varphi_1+\theta_1) - r_0\cos(\theta_0) - 2M = 0 \\ M - \frac{2n^2RI_n}{V_{in}T_s\omega_{r0}}[r_0\cos(\theta_0) - r_0\cos(\varphi_0+\theta_0) \\ +r_1\cos(\theta_1) - r_1\cos(\varphi_1+\theta_1)] = 0 \\ \varphi_0 + \varphi_1 - \frac{\omega_{r0}T_s}{2} = 0 \end{cases}. \tag{15}$$

III. A SMALL SIGNAL MODELING OF THE *LLC* CONVERTER BASED ON TIME-DOMAIN ANALYSIS

LLC resonant converter is typically controlled by PFM. The influence of input voltage and switching frequency on the output voltage can be visualized on the state plane, altering the planar trajectory and affecting the quiescent operating point. In the steady state, when the initial resonant current i_{r0N} or resonant capacitor voltage v_{cr0N} at t_0 are disturbed respectively, the trajectory in a switching period will not be closed curves, and the output voltage will be affected as well. The disturbed trajectories are shown in Fig. 4. Therefore, perturbations are introduced to i_{r0N} and v_{cr0N}, which can reflect the influence of input voltage and switching frequency on the state trajectory. Consequently, in order to analyze the small-signal model of the *LLC* resonant converter, the initial values of the resonant current i_{r0N} and the resonant capacitor voltage v_{cr0N} can also be regarded as the state variables besides the output voltage v_o, and the input voltage v_{in} and switching period t_s are taken as the input variables of the system.

A. Small Signal Modeling for $f_s < f_r$

Because i_{r0N} and v_{cr0N} in the next switching period are i_{r6N} and v_{cr6N} in the current period, the large signal model of the system can be obtained as shown in

$$\begin{cases} \dot{i}_{r0N} = \dfrac{i_{r6N} - i_{r0N}}{t_s} \\ \qquad = \frac{1}{t_s}\left[\dfrac{r_3}{\sqrt{1+L_n}}\sin(\varphi_3+\theta_3) - r_0\sin(\theta_0)\right] \\ \dot{v}_{cr0N} = \dfrac{v_{cr6N} - v_{cr0N}}{t_s} \\ \qquad = \frac{1}{t_s}\left[-r_3\cos(\varphi_3+\theta_3) + r_0\cos(\theta_0) - (2-M)\right] \\ \dot{v}_o = \frac{1}{C_o}\left(\dot{i}_{\text{rec}} - \frac{v_o}{R}\right) \end{cases}. \tag{16}$$

Section II provides the calculation method for the steady-state operating point. Therefore, the steady-state values of I_{r0N}, V_{cr0N}, M, V_{in}, V_o, T_s, r_0, θ_0, φ_0, I_{r2N}, etc., can be obtained. The perturbation-linearization method is used to build the small-signal model of the *LLC* resonant converter. The main idea is to add perturbations $\hat{v}_{in}$, $\hat{v}_o$, $\hat{t}_s$, $\hat{i}_{r0N}$, and $\hat{v}_{cr0N}$ to V_{in}, V_o, T_s, I_{r0N}, and V_{cr0N} at the steady-state operating point, as shown in (17), and then gradually derive the variations of i_{r6N}, v_{cr6N}, and $\bar{i}_{rec}$ at t_6

$$\begin{cases} v_{\text{in}} = V_{\text{in}} + \hat{v}_{\text{in}} \\ v_o = V_o + \hat{v}_o \\ t_s = T_s + \hat{t}_s \\ i_{r0N} = I_{r0N} + \hat{i}_{r0N} \\ v_{cr0N} = V_{cr0N} + \hat{v}_{cr0N} \end{cases}. \tag{17}$$

When the state variables are disturbed, both the initial phase θ_0 and the state trajectory radius r_0 change accordingly. The Taylor's expansions of (1) and (2) are carried out at the steady-state operating point. The variations $\Delta\theta_0$ and Δr_0 can be obtained respectively by reserving only the first-order components of Taylor's expansions and ignoring the higher-order components, as shown in (18) and (19). g and h represent the partial derivatives of the phase θ and radius r to the corresponding variables, respectively. The steady-state operating point is substituted into the partial detivatives, which are shown in the following:

$$\begin{aligned} \Delta\theta_0 &= \frac{\partial\theta_0}{\partial i_{r0N}}\hat{i}_{r0N} + \frac{\partial\theta_0}{\partial v_{cr0N}}\hat{v}_{cr0N} + \frac{\partial\theta_0}{\partial v_{\text{in}}}\hat{v}_{\text{in}} + \frac{\partial\theta_0}{\partial v_o}\hat{v}_o \\ &= g_{0i}\hat{i}_{r0N} + g_{0v}\hat{v}_{cr0N} + g_{0\text{in}}\hat{v}_{\text{in}} + g_{0o}\hat{v}_o \end{aligned} \tag{18}$$

where

$$g_{0i} = \frac{\partial\theta_0}{\partial i_{r0N}} = -\frac{V_{cr0N} - (1-M)}{[V_{cr0N} - (1-M)]^2 + {I_{r0N}}^2}$$

$$g_{0v} = \frac{\partial\theta_0}{\partial v_{cr0N}} = \frac{I_{r0N}}{[V_{cr0N} - (1-M)]^2 + {I_{r0N}}^2}$$

$$g_{0in} = \frac{\partial\theta_0}{\partial v_{in}} = -\frac{I_{r0N}M/V_{in}}{[V_{cr0N} - (1-M)]^2 + {I_{r0N}}^2}$$

$$g_{0o} = \frac{\partial\theta_0}{\partial v_o} = \frac{nI_{r0N}/V_{in}}{[V_{cr0N} - (1-M)]^2 + {I_{r0N}}^2}$$

$$\begin{aligned} \Delta r_0 &= \frac{\partial r_0}{\partial i_{r0N}}\hat{i}_{r0N} + \frac{\partial r_0}{\partial v_{cr0N}}\hat{v}_{cr0N} + \frac{\partial r_0}{\partial v_{\text{in}}}\hat{v}_{\text{in}} + \frac{\partial r_0}{\partial v_o}\hat{v}_o \\ &= h_{0i}\hat{i}_{r0N} + h_{0v}\hat{v}_{cr0N} + h_{0\text{in}}\hat{v}_{\text{in}} + h_{0o}\hat{v}_o \end{aligned} \tag{19}$$

where

$$h_{0i} = \frac{\partial\theta_0}{\partial i_{r0N}} = \frac{I_{r0N}}{\sqrt{{I_{r0N}}^2 + [V_{cr0N} - (1-M)]^2}}$$

$$h_{0v} = \frac{\partial\theta_0}{\partial v_{cr0N}} = \frac{V_{cr0N} - (1-M)}{\sqrt{{I_{r0N}}^2 + [V_{cr0N} - (1-M)]^2}}$$

$$h_{0in} = \frac{\partial\theta_0}{\partial v_{in}} = \frac{[V_{cr0N} - (1-M)]M/v_{in}}{\sqrt{{I_{r0N}}^2 + [V_{cr0N} - (1-M)]^2}}$$

$$h_{0o} = \frac{\partial\theta_0}{\partial v_o} = \frac{[V_{cr0N} - (1-M)]n/v_{in}}{\sqrt{{I_{r0N}}^2 + [V_{cr0N} - (1-M)]^2}}.$$

After adding the perturbations, the resonant current is equal to the magnetizing current at $t_2+\Delta t_2$. At this time, the current i_{sN} on the secondary side is zero, i.e., $i_{sN}(t_2+\Delta t_2) = 0$. Therefore, (20) can be obtained by linearizing (11) at t_2. Therefore, $\Delta\varphi_0$ can be obtained as shown in (21), where m represents the partial derivative of φ to the perturbation variables

$$\begin{aligned} i_{sN}(t_2+\Delta t_2) = i_{sN}(t_2) &+ \frac{\partial i_{sN}(t_2)}{\partial r_0}\Delta r_0 + \frac{\partial i_{sN}(t_2)}{\partial\varphi_0}\Delta\varphi_0 \\ &+ \frac{\partial i_{sN}(t_2)}{\partial\theta_0}\Delta\theta_0 + \frac{\partial i_{sN}(t_2)}{\partial v_{in}}\hat{v}_{in} \\ &+ \frac{\partial i_{sN}(t_2)}{\partial v_o}\hat{v}_o = 0 \end{aligned} \tag{20}$$

$$\Delta\varphi_0 = m_{0i}\hat{i}_{r0N} + m_{0v}\hat{v}_{cr0N} + m_{0\text{in}}\hat{v}_{\text{in}} + m_{0o}\hat{v}_o. \tag{21}$$

Linearizing (3) and substituting (18), (19), and (21) into the linearizing results, Δi_{r2N} and Δv_{cr2N} are shown in (22), where k and l represent the partial derivatives of the resonant current and the resonant capacitor voltage to the perturbation variables, respectively,

$$\begin{cases} \Delta i_{r2N} = k_{2i}\hat{i}_{r0N} + k_{2v}\hat{v}_{cr0N} + k_{2\text{in}}\hat{v}_{\text{in}} + k_{2o}\hat{v}_o \\ \Delta v_{cr2N} = l_{2i}\hat{i}_{r0N} + l_{2v}\hat{v}_{cr0N} + l_{2\text{in}}\hat{v}_{in} + l_{2o}\hat{v}_o \end{cases}. \tag{22}$$

The expressions for $\Delta\theta_1$ and Δr_1 can be obtained according to (4) and (5), as shown in

$$\begin{cases} \Delta\theta_1 = g_{1i}\hat{i}_{r0N} + g_{1v}\hat{v}_{cr0N} + g_{1\text{in}}\hat{v}_{\text{in}} + g_{1o}\hat{v}_o \\ \Delta r_1 = h_{1i}\hat{i}_{r0N} + h_{1v}\hat{v}_{cr0N} + h_{1\text{in}}\hat{v}_{\text{in}} + h_{1o}\hat{v}_o \end{cases}. \tag{23}$$

From t_0 to t_3, $\Delta\varphi_1$ can be expressed as

$$\Delta\varphi_1 = \frac{\omega_{r1}}{2}\hat{t}_s - \frac{\omega_{r1}}{\omega_{r0}}\Delta\varphi_0. \tag{24}$$

Then, (25) can be derived from (6)

$$\begin{cases} \Delta i_{r3N} = k_{3i}\hat{i}_{r0N} + k_{3v}\hat{v}_{cr0N} + k_{3\text{in}}\hat{v}_{\text{in}} + k_{3o}\hat{v}_o + k_{3t}\hat{t}_s \\ \Delta v_{cr3N} = l_{3i}\hat{i}_{r0N} + l_{3v}\hat{v}_{cr0N} + l_{3\text{in}}\hat{v}_{\text{in}} + l_{3o}\hat{v}_o + l_{3t}\hat{t}_s \end{cases}. \tag{25}$$

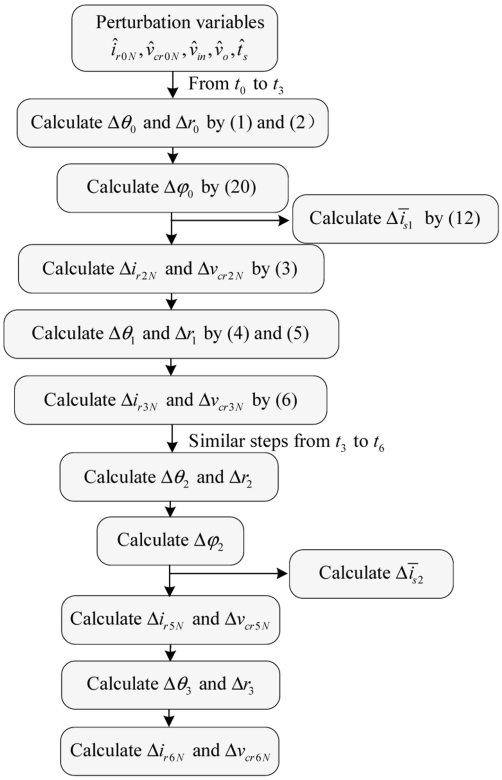

Fig. 5. Flowchart of the whole derivation process for $f_s < f_r$.

The variation of the average current $\Delta\bar{i}_{s1}$ on the secondary side in the half period from t_0 to t_3 is shown in (26) by linearizing (12)

$$\Delta\bar{i}_{s1} = k_{s1i}\hat{i}_{r0N} + k_{s1v}\hat{v}_{cr0N} + k_{s1\text{in}}\hat{v}_{\text{in}} + k_{s1o}\hat{v}_o + k_{s1t}\hat{t}_s. \tag{26}$$

Because of the semiperiod symmetry, similar procedures can be used to deduce the variations from t_3 to t_6. Then, the variations Δi_{r6N} and Δv_{cr6N} are expressed as

$$\begin{cases} \Delta i_{r6N} = k_{6i}\hat{i}_{r0N} + k_{6v}\hat{v}_{cr0N} + k_{6\text{in}}\hat{v}_{\text{in}} + k_{6o}\hat{v}_o + k_{6t}\hat{t}_s \\ \Delta v_{cr6N} = l_{6i}\hat{i}_{r0N} + l_{6v}\hat{v}_{cr0N} + l_{6\text{in}}\hat{v}_{\text{in}} + l_{6o}\hat{v}_o + l_{6t}\hat{t}_s \end{cases}. \tag{27}$$

The variation of the average current in the secondary winding $\Delta\bar{i}_{s2}$ in the second half cycle from t_3 to t_6 is expressed as

$$\Delta\bar{i}_{s2} = k_{s2i}\hat{i}_{r0N} + k_{s2v}\hat{v}_{cr0N} + k_{s2\text{in}}\hat{v}_{\text{in}} + k_{s2o}\hat{v}_o + k_{s2t}\hat{t}_s. \tag{28}$$

The flowchart of the whole derivation process for $f_s < f_r$ is shown in Fig. 5. During the whole switching cycle, the variation of the average output current of the rectifier bridge can be expressed as

$$\begin{aligned} \Delta\bar{i}_{\text{rec}} &= \Delta\bar{i}_{s1} - \Delta\bar{i}_{s2} \\ &= (k_{s1i} - k_{s2i})\,\hat{i}_{r0N} + (k_{s1v} - k_{s2v})\,\hat{v}_{cr0N} \\ &\quad + (k_{s1o} - k_{s2o})\,\hat{v}_o + (k_{s1\text{in}} - k_{s2\text{in}})\,\hat{v}_{\text{in}} + (k_{s1t} - k_{s2t})\,\hat{t}_s. \end{aligned} \tag{29}$$

By substituting (17) into (16), (30) can be obtained

$$\begin{cases} \left(I_{r0N} + \hat{i}_{r0N}\right)^{\cdot} = \dfrac{I_{r6N} + \Delta i_{r6N} - I_{r0N} - \hat{i}_{r0N}}{T_s + \hat{t}_s} \\ \left(V_{cr0N} + \hat{v}_{cr0N}\right)^{\cdot} = \dfrac{V_{cr6N} + \Delta v_{cr6N} - V_{cr0N} - \hat{v}_{cr0N}}{T_s + \hat{t}_s} \\ \left(V_o + \hat{v}_o\right)^{\cdot} = \dfrac{1}{C_o}\left(\bar{i}_{\text{rec}} + \Delta\bar{i}_{\text{rec}} - \frac{V_o}{R} - \frac{\hat{v}_o}{R}\right) \end{cases}. \tag{30}$$

The equations in (30) can be extended by using Taylor series expansions and retaining the first-order components. Substituting (27) and (29) into (30), (31) can be obtained as

$$\begin{aligned} \dot{\hat{i}}_{r0N} &= \frac{\Delta i_{r6N} - \hat{i}_{r0N}}{T_s} = \frac{1}{T_s}\left[(k_{6i} - 1)\,\hat{i}_{r0N} + k_{6v}\hat{v}_{cr0N}\right. \\ &\quad \left. + k_{6\text{in}}\hat{v}_{\text{in}} + k_{6o}\hat{v}_o + k_{6t}\hat{t}_s\right] \\ \dot{\hat{v}}_{cr0N} &= \frac{\Delta v_{cr6N} - \hat{v}_{cr0N}}{T_s} = \frac{1}{T_s}\left[l_{6i}\hat{i}_{r0N} + (l_{6v} - 1)\,\hat{v}_{cr0N}\right. \\ &\quad \left. + l_{6\text{in}}\hat{v}_{\text{in}} + l_{6o}\hat{v}_o + l_{6t}\hat{t}_s\right] \\ \dot{\hat{v}}_o &= \frac{1}{C_o}\left(\Delta\bar{i}_{rec} - \frac{\hat{v}_o}{R}\right) \\ &= \frac{1}{C_o}\begin{pmatrix} (k_{s1i} - k_{s2i})\,\hat{i}_{r0N} + (k_{s1v} - k_{s2v})\,\hat{v}_{cr0N} \\ + \left(k_{s1o} - k_{s2o} - \frac{1}{R}\right)\hat{v}_o + (k_{s1\text{in}} - k_{s2in})\,\hat{v}_{\text{in}} \\ + (k_{s1t} - k_{s2t})\,\hat{t}_s \end{pmatrix}. \end{aligned} \tag{31}$$

Setting $u = [\hat{v}_{\text{in}}, \hat{t}_s]$, $x = [\hat{i}_{r0N}, \hat{v}_{cr0N}, \hat{v}_o]$ and $y = \hat{v}_o$, the above equations can be expressed as (32), where the state matrix A, the input matrix B, and the output matrix C are shown as

$$\begin{aligned} \dot{x} &= Ax + Bu \\ y &= Cx \end{aligned} \tag{32}$$

$$A = \begin{bmatrix} \dfrac{k_{6i} - 1}{T_s} & \dfrac{k_{6v}}{T_s} & \dfrac{k_{6o}}{T_s} \\ \dfrac{l_{6i}}{T_s} & \dfrac{l_{6v} - 1}{T_s} & \dfrac{l_{6o}}{T_s} \\ \dfrac{k_{s1i} - k_{s2i}}{C_o} & \dfrac{k_{s1v} - k_{s2v}}{C_o} & \dfrac{k_{s1o} - k_{s2o} - 1/R}{C_o} \end{bmatrix}$$

$$B = \begin{bmatrix} \dfrac{k_{6\text{in}}}{T_s} & \dfrac{k_{6t}}{T_s} \\ \dfrac{l_{6\text{in}}}{T_s} & \dfrac{l_{6t}}{T_s} \\ \dfrac{k_{s1\text{in}} - k_{s2\text{in}}}{C_o} & \dfrac{k_{s1t} - k_{s2t}}{C_o} \end{bmatrix}$$

$$C = \begin{bmatrix} 0 & 0 & 1 \end{bmatrix} \tag{33}$$

According to (32), the transfer function of the *LLC* converter for $f_s < f_r$ can be expressed as

$$G(s) = C(sI - A)^{-1}B = \begin{bmatrix} G_{v\text{in}}(s) & G_t(s) \end{bmatrix} \tag{34}$$

where G is a 1×2 matrix. $G_{v\text{in}}(s)$ is the transfer function from the input voltage to the output voltage, and $G_t(s)$ is

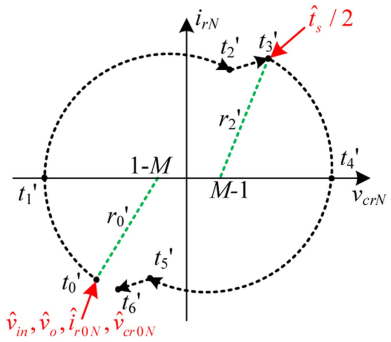

Fig. 6. Diagram of periodic perturbation lag $T_s/2$.

the transfer function from the switching period to the output voltage.

As shown in Fig. 6, during the derivation of the small-signal model, perturbations $\hat{v}_{\text{in}}$, $\hat{v}_o$, $\hat{i}_{r0N}$, and $\hat{v}_{cr0N}$ are introduced at t_0, and they have an impact on the state trajectory in the whole switching period. However, switching period perturbation $\hat{t}_s$ comes into effect at t_3, resulting in a phase lag of half a switching period. Considering the time delay of $T_s/2$, the transfer function from the switching period to the output voltage is revised to

$$G_{ts}(s) = G_t(s) \cdot e^{-\frac{T_s}{2}s}. \tag{35}$$

Since $t_s = 1/f_s$, the relationship between the perturbation of the switching period and the perturbation of the switching frequency is shown in (36). Therefore, the transfer function from the switching frequency to the output voltage can be obtained as

$$\hat{t}_s = -\frac{1}{{f_s}^2}\hat{f}_s \tag{36}$$

$$G_{fs}(s) = -\frac{1}{{f_s}^2}G_{ts}(s). \tag{37}$$

B. Small Signal Modeling for $f_s > f_r$

The derivation process of the small-signal model for $f_s > f_r$ is similar to that for $f_s < f_r$. $\Delta\theta_0$ and Δr_0 are shown in (18) and (19). Δi_{r2N} and Δv_{cr2N} are shown in (38) by linearizing (3), and $\Delta\varphi_0$ needs to be solved

$$\begin{cases} \Delta i_{r2N} = k_{2i}\hat{i}_{r0N} + k_{2v}\hat{v}_{cr0N} + k_{2\text{in}}\hat{v}_{\text{in}} + k_{2o}\hat{v}_o + k_{2m0}\Delta\varphi_0 \\ \Delta v_{cr2N} = l_{2i}\hat{i}_{r0N} + l_{2v}\hat{v}_{cr0N} + l_{2\text{in}}\hat{v}_{\text{in}} + l_{2o}\hat{v}_o + l_{2m0}\Delta\varphi_0 \end{cases}. \tag{38}$$

According to (7) and (8), it can be derived that $\Delta\theta_1$ and Δr_1 are associated with the perturbation variables and $\Delta\varphi_0$ as shown in

$$\begin{cases} \Delta\theta_1 = g_{1i}\hat{i}_{r0N} + g_{1v}\hat{v}_{cr0N} + g_{1\text{in}}\hat{v}_{\text{in}} + g_{1o}\hat{v}_o + g_{1m0}\Delta\varphi_0 \\ \Delta r_1 = h_{1i}\hat{i}_{r0N} + h_{1v}\hat{v}_{cr0N} + h_{1\text{in}}\hat{v}_{\text{in}} + h_{1o}\hat{v}_o + h_{1m0}\Delta\varphi_0 \end{cases}. \tag{39}$$

Because $i_{sN}(t_3) = 0$ at t_3, $i_{sN}(t_3+\Delta t_3)$ must be also equal to zero at $t_3+\Delta t_3$, Therefore, (40) can be obtained as

$$\begin{aligned} \Delta i_{sN}(t_3+\Delta t_3) &= i_{sN}(t_3+\Delta t_3) - i_{sN}(t_3) \\ &= \frac{\partial i_{sN}(t_3)}{\partial r_0}\Delta r_0 + \frac{\partial i_{sN}(t_3)}{\partial r_1}\Delta r_1 \\ &+ \frac{\partial i_{sN}(t_3)}{\partial \varphi_1}\Delta\varphi_1 + \frac{\partial i_{sN}(t_3)}{\partial \theta_0}\Delta\theta_0 \\ &+ \frac{\partial i_{sN}(t_3)}{\partial \theta_1}\Delta\theta_1 + \frac{\partial i_{sN}(t_3)}{\partial v_{\text{in}}}\hat{v}_{\text{in}} \\ &+ \frac{\partial i_{sN}(t_3)}{\partial v_o}\hat{v}_o + \frac{\partial i_{sN}(t_3)}{\partial t_s}\hat{t}_s = 0. \end{aligned} \tag{40}$$

From t_0 to t_3, the relationship between $\Delta\varphi_0$ and $\Delta\varphi_1$ in half a switching cycle can be expressed as

$$\Delta\varphi_0 + \Delta\varphi_1 = \frac{\omega_{r0}}{2}\hat{t}_s. \tag{41}$$

Combining (18) and (19) and (39) and (41), $\Delta\varphi_1$ and $\Delta\varphi_0$ can be solved as

$$\begin{cases} \Delta\varphi_1 = m_{1i}\hat{i}_{r0N} + m_{1v}\hat{v}_{cr0N} + m_{1\text{in}}\hat{v}_{\text{in}} + m_{1o}\hat{v}_o + m_{1t}\hat{t}_s \\ \Delta\varphi_0 = \frac{\omega_{r0}}{2}\hat{t}_s - \Delta\varphi_1 \end{cases}. \tag{42}$$

Substituting (42) into (38) and (39), Δi_{r2N}, Δv_{cr2N}, $\Delta\theta_1$, and Δr_1 associated with $\hat{v}_{\text{in}}$, $\hat{v}_o$, $\hat{t}_s$, $\hat{i}_{r0N}$, and$\hat{v}_{cr0N}$ can be determined. The expressions for Δi_{r3N} and Δv_{cr3N} can be obtained as shown in (43) by taking a partial derivative of (9)

$$\begin{cases} \Delta i_{r3N} = k_{3i}\hat{i}_{r0N} + k_{3v}\hat{v}_{cr0N} + k_{3\text{in}}\hat{v}_{\text{in}} + k_{3o}\hat{v}_o + k_{3t}\hat{t}_s \\ \Delta v_{cr3N} = l_{3i}\hat{i}_{r0N} + l_{3v}\hat{v}_{cr0N} + l_{3\text{in}}\hat{v}_{\text{in}} + l_{3o}\hat{v}_o + l_{3t}\hat{t}_s \end{cases}. \tag{43}$$

The expression $\Delta\bar{i}_{s1}$ on the secondary side of the transformer during the half of the switching cycle from t_0 to t_3 is shown as

$$\begin{aligned} \Delta\bar{i}_{s1} &= \frac{\partial\bar{i}_{s1}}{\partial r_0}\Delta r_0 + \frac{\partial\bar{i}_{s1}}{\partial\theta_0}\Delta\theta_0 + \frac{\partial\bar{i}_{s1}}{\partial\varphi_0}\Delta\varphi_0 + \frac{\partial\bar{i}_{s1}}{\partial r_1}\Delta r_1 \\ &+ \frac{\partial\bar{i}_{s1}}{\partial\theta_1}\Delta\theta_1 + \frac{\partial\bar{i}_{s1}}{\partial\varphi_1}\Delta\varphi_1 + \frac{\partial\bar{i}_{s1}}{\partial v_{\text{in}}}\hat{v}_{\text{in}} + \frac{\partial\bar{i}_{s1}}{\partial t_s}\hat{t}_s \\ &= k_{s1i}\hat{i}_{r0N} + k_{s1v}\hat{v}_{cr0N} + k_{s1\text{in}}\hat{v}_{\text{in}} + k_{s1o}\hat{v}_o + k_{s1t}\hat{t}_s. \end{aligned} \tag{44}$$

From t_3 to t_6, a similar procedure can be used to obtain the expressions for Δi_{r6N}, Δv_{cr6N}, and $\Delta\bar{i}_{\text{rec}}$. Due to the similarity between the derivation process of the small-signal model for $f_s < f_r$ and $f_s > f_r$, the derivation process for $f_s > f_r$ can be referenced from Fig. 6. The small-signal model of the *LLC* converter and the transfer function for $f_s > f_r$ can be obtained by referring to (30)–(37).

IV. Small Signal Modeling of the *LLC* Converter in Time-Shift Control

A. Analysis of the Time-Shift Control

Due to the resonant converter operating in the inductive region, energy continues to flow out of the resonant tank after the switches are turned on at t_0 and t_3. Only after the resonant current crosses zero at t_1 and t_4, energy in the input source flows into the resonant tank, lasting until the switches are turned off at t_3 or t_6. This period is denoted as t_{cs}, as illustrated in Fig. 7. TSC,

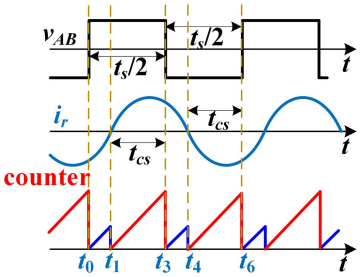

Fig. 7. Diagram of *LLC* time-shift control.

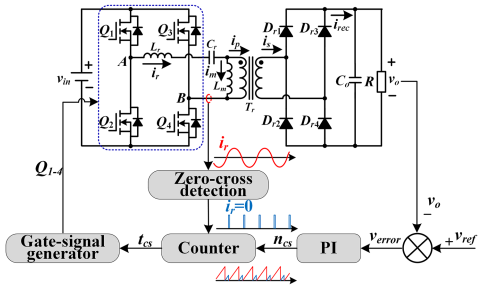

Fig. 8. Closed-loop control block diagram of TSC.

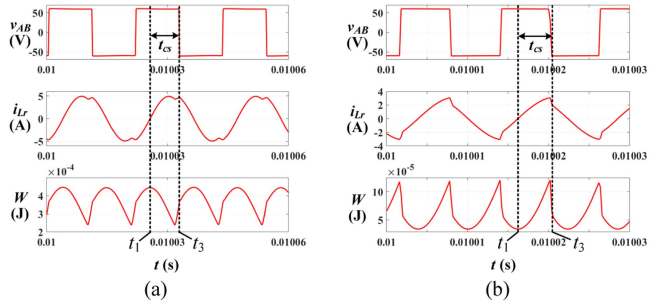

Fig. 9. Simulation of energy stored in the *LC* resonant tank. (a) $f_s < f_r$. (b) $f_s > f_r$.

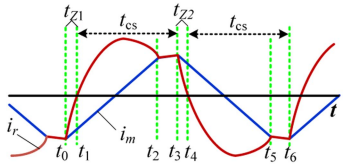

Fig. 10. Analysis of control time under TSC for $f_s < f_r$.

distinct from PFM, directly regulates the duration t_{cs} during which energy flows into the resonant tank to adjust the output voltage.

Furthermore, the TSC method is also easily implementable in the digital controller, as shown in Fig. 7. The zero-crossing detection of the resonant current can be realized by using an analog circuit to determine t_1 and t_4. The time base counter starts at the beginning of the switching period. When the resonant current crosses zero at t_1 and t_4, the time base counter is reset to zero. Therefore, t_{cs} is equivalent to controlling the amplitude of the time base counter. The closed-loop control block diagram of TSC is shown in Fig. 8.

As seen in half of the trajectories from t_0 to t_2 for both $f_s < f_r$ and $f_s > f_r$, the resonant inductor L_r and resonant capacitor C_r are in resonance. The instantaneous energy stored in the *LC* resonant tank during t_0 to t_2 is expressed as

$$\begin{aligned} W &= \frac{1}{2}L_r {i_r}^2 + \frac{1}{2}C_r {v_r}^2 \\ &= \frac{1}{2}C_r {V_{\text{in}}}^2 [r_0 \sin(\varphi + \theta_0)]^2 \\ &\quad + \frac{1}{2}C_r {V_{\text{in}}}^2 [-r_0 \cos(\varphi + \theta_0) + (1 - M)]^2. \end{aligned} \tag{45}$$

Differentiating W to φ, the expression is shown in (46). Solving (46), φ is equal to -θ_0, which indicates that the energy stored in the *LC* resonant tank gets the extreme value at t_1. At this time, the resonant current is equal to zero

$$\frac{dW}{d\varphi} = C_r {V_{\text{in}}}^2 r_0 (1 - M) \sin(\varphi + \theta_0) = 0. \tag{46}$$

The simulation of the energy stored in the *LC* resonant tank is shown in Fig. 9. For $f_s < f_r$, the energy stored in the *LC* resonant tank reaches the maximum at t_1. For $f_s > f_r$, the energy stored in the *LC* resonant tank reaches the minimum at t_1. Therefore, the time interval t_{cs} reflects the energy variation transmitted from the input voltage into the *LLC* converter and can be used as the variable for the current mode control. The above analysis reveals the reason why the TSC can be regarded as current mode control.

The small-signal modeling for TSC is based on the analysis presented in Section III. By building the relationship between the perturbation of the control time t_{cs} and the perturbation of the switching period t_s, the small-signal model can be derived.

B. Small Signal Modeling of the LLC *Converter in Time-Shift Control for $f_s < f_r$*

As shown in Fig. 10, t_1-t_0 is designated as t_{Z1}, and t_4-t_3 is designated as t_{Z2}. According to the analysis of the state trajectory in Section II, it can be derived that t_{Z1} = -θ_0/ω_{r0} and $t_{Z2} = (\pi\text{-}\theta_2)/\omega_{r0}$.

By introducing the perturbation, the variations Δt_{Z1} and Δt_{Z2} can be expressed as

$$\begin{cases} \Delta t_{Z1} = -\frac{\Delta\theta_0}{\omega_{r0}} \\ \qquad = -\frac{1}{\omega_{r0}}\left(g_{0i}\hat{i}_{r0N} + g_{0v}\hat{v}_{cr0N} + g_{0\text{in}}\hat{v}_{\text{in}} + g_{0o}\hat{v}_o\right) \\ \Delta t_{Z2} = -\frac{\Delta\theta_2}{\omega_{r0}} \\ \qquad = -\frac{1}{\omega_{r0}}\left(g_{2i}\hat{i}_{r0N} + g_{2v}\hat{v}_{cr0N} + g_{2\text{in}}\hat{v}_{\text{in}} \right. \\ \qquad\quad \left. + g_{2o}\hat{v}_o + g_{2t}\hat{t}_s\right) \end{cases} . \tag{47}$$

Within one switching cycle, t_s is equal to $2t_{cs}$+t_{Z1}+t_{Z2}. Therefore, the relationship between perturbation of the control time t_{cs} and perturbation of the switching period t_s can be expressed as

$$\hat{t}_s = 2\hat{t}_{cs} + \Delta t_{Z1} + \Delta t_{Z2}. \tag{48}$$

According to (48), $\hat{t}_s$ can be rewritten as

$$\hat{t}_s = A_Z \hat{x} + B_Z \begin{bmatrix} \hat{v}_{\text{in}} \\ \hat{t}_{cs} \end{bmatrix} \tag{49}$$

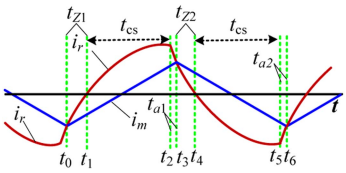

Fig. 11. Analysis of control time under TSC for $f_s > f_r$.

where

$$A_Z = \frac{1}{\omega_{r0} + g_{2t}} \begin{bmatrix} -g_{0i} - g_{2i} & -g_{0v} - g_{2v} & -g_{0o} - g_{2o} \end{bmatrix}$$

$$B_Z = \frac{1}{\omega_{r0} + g_{2t}} \begin{bmatrix} -g_{0\text{in}} - g_{2\text{in}} & 2\omega_{r0} \end{bmatrix}.$$

Substituting (49) into (32), (32) can be rewritten as

$$\dot{\hat{x}} = A\hat{x} + \begin{bmatrix} B_1 & B_2 \end{bmatrix} \begin{bmatrix} \hat{v}_{\text{in}} \\ \hat{t}_s \end{bmatrix} = A_c\hat{x} + B_c \begin{bmatrix} \hat{v}_{\text{in}} \\ \hat{t}_{cs} \end{bmatrix} \tag{50}$$

where

$$A_c = A + B_2 A_Z$$

$$B_c = \begin{bmatrix} B_1 + B_2 \frac{-g_{0\text{in}} - g_{2\text{in}}}{\omega_{r0} + g_{2t}} & \frac{2\omega_{r0}}{\omega_{r0} + g_{2t}} B_2 \end{bmatrix}.$$

Therefore, the transfer function under the TSC can be obtained according to (51) for $f_s < f_r$. $G_{tc}(s)$ is the transfer function from the control time t_{cs} to the output voltage v_o. Considering the time delay in Fig. 6, the transfer function from the control time t_{cs} to the output voltage v_o is revised to (52)

$$G_{cs}(s) = C(sI - A_c)^{-1} B_c = \begin{bmatrix} G_{vin}(s) & G_{tc}(s) \end{bmatrix} \tag{51}$$

$$G_{tcs}(s) = G_{tc}(s)\, e^{-\frac{T_s}{2}}. \tag{52}$$

C. Small Signal Modeling of the LLC Converter in Time-Shift Control for $f_s > f_r$

As depicted in Fig. 11, the half of the switching cycle is from t_0 to t_3. It can be divided into three parts, including t_1-t_0, t_2-t_1, and t_3-t_2. They are designated as t_{Z1}, t_{cs}, and t_{a1} respectively. Similarly, the half cycle from t_3 to t_6 can be divided into t_{Z2}, t_{cs}, and t_{a2}. Based on the analysis of the state trajectory for $f_s > f_r$ in Section II, it can be obtained that $t_{Z1} = \text{-}\theta_0/\omega_{r0}$, $t_{Z2} = (\pi\text{-}\theta_2)/\omega_{r0}$, $t_{a1} = \varphi_1/\omega_{r0}$ and $t_{a2} = \varphi_3/\omega_{r0}$.

The variations Δt_{Z1} and Δt_{Z2} can be obtained by (47), and Δt_{a1} and Δt_{a2} can be expressed as

$$\begin{cases} \Delta t_{a1} = \frac{\Delta\varphi_1}{\omega_{r0}} = \frac{1}{\omega_{r0}} \left(m_{1i}\hat{i}_{r0N} + m_{1v}\hat{v}_{cr0N} + m_{1\text{in}}\hat{v}_{\text{in}} + m_{1o}\hat{v}_o + m_{1t}\hat{t}_s \right) \\ \Delta t_{a2} = \frac{\Delta\varphi_3}{\omega_{r0}} = \frac{1}{\omega_{r0}} \left(m_{3i}\hat{i}_{r0N} + m_{3v}\hat{v}_{cr0N} + m_{3\text{in}}\hat{v}_{\text{in}} + m_{3o}\hat{v}_o + m_{3t}\hat{t}_s \right) \end{cases}. \tag{53}$$

In a whole switching cycle, t_s is equal to $t_{Z1} + t_{Z2} + t_{a1} + t_{a2} + 2t_{cs}$. Therefore, (54) can be obtained as

$$\hat{t}_s = \Delta t_{Z1} + 2\hat{t}_{cs} + \Delta t_{Z2} + \Delta t_{a1} + \Delta t_{a2}. \tag{54}$$

TABLE II
CIRCUIT PARAMETERS

Items	Symbols	Parameters
Input dc voltage	V_{in}	60 V
Resonant inductor	L_r	24 μH
Resonant capacitor	C_r	365 nF
Magnetizing inductor	L_m	75 μH
Resonant frequency	f_r	53.7 kHz
Turns ratio of the transformer	n	1
Load resistance	R	40 Ω
Input filter capacitor	C_{in}	1410 μF
Output filter capacitor	C_o	36 μF

In terms of (54), the relationship between the perturbations $\hat{t}_s$ and $\hat{t}_{cs}$ can be shown as

$$\hat{t}_s = A_Z \begin{bmatrix} \hat{i}_{r0N} \\ \hat{v}_{r0N} \\ \hat{v}_o \end{bmatrix} + B_Z \begin{bmatrix} \hat{v}_{\text{in}} \\ \hat{t}_{cs} \end{bmatrix} \tag{55}$$

where

$$A_Z = \frac{1}{\omega_{r0} + g_{2t} - m_{1t} - m_{3t}} \begin{bmatrix} (-g_{0i} - g_{2i} + m_{1i} + m_{3i}) \\ (-g_{0v} - g_{2v} + m_{1v} + m_{3v}) \\ (-g_{0o} - g_{2o} + m_{1o} + m_{3o}) \end{bmatrix}^T$$

$$B_Z = \frac{1}{\omega_{r0} + g_{2t} - m_{1t} - m_{3t}} \times \begin{bmatrix} (-g_{0\text{in}} - g_{2\text{in}} + m_{1\text{in}} + m_{3\text{in}}) & 2\omega_{r0} \end{bmatrix}.$$

By substituting (55) into (32), the equation of states for $f_s > f_r$ is also shown in the form of (50), where

$$A_c = A + B_2 A_Z$$

$$B_c = \begin{bmatrix} B_1 + \frac{-g_{0\text{in}} - g_{2\text{in}} + m_{1\text{in}} + m_{3\text{in}}}{\omega_{r0} + g_{2t} - m_{1t} - m_{3t}} B_2 \\ \frac{2\omega_{r0}}{\omega_{r0} + g_{2t} - m_{1t} - m_{3t}} B_2 \end{bmatrix}^T.$$

Similarly, the transfer function under the TSC for $f_s > f_r$ can be obtained according to (51) and (52).

D. Frequency-Domain Modeling Comparisons of the LLC Converter in PFM and TSC

The simulation model of the *LLC* resonant converter is built in PSIM software, and the circuit parameters are given in Table II with 53.7 kHz resonant frequency.

The frequency ac sweep under PFM is carried out at the steady-state operating points with switching frequencies of 43, 48, 60, and 65 kHz. The frequency response of the open loop can be obtained by a small ac excitation signal injected into the switching frequency as the perturbation. The theoretical model and simulation results of the bode diagram from the switching period to the output voltage are shown in Fig. 12. It can be observed that the theoretical model agrees well with the simulation data in terms of amplitude gain and phase for $f_s < f_r$ and $f_s > f_r$, validating the effectiveness of the small signal modeling of the *LLC* under PFM. In PFM, the frequency response is close to the second-order system. The phase of the

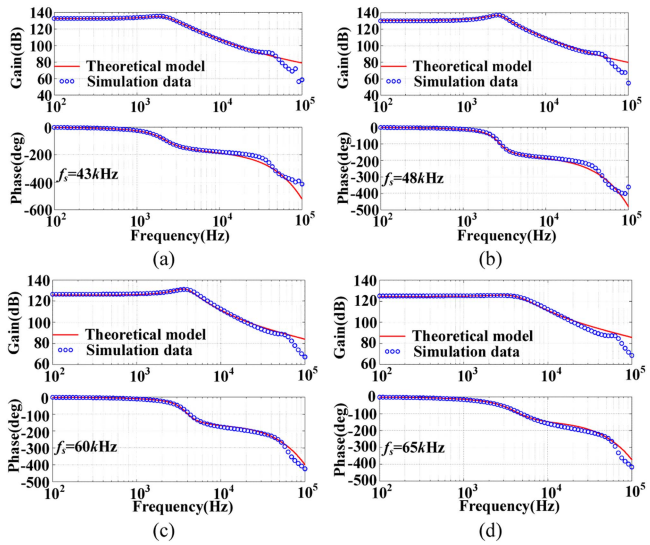

Fig. 12. Simulation results and theoretical model from the switching period to the output voltage under PFM. (a) $f_s = 43$ kHz. (b) $f_s = 48$ kHz. (c) $f_s = 60$ kHz. (d) $f_s = 65$ kHz.

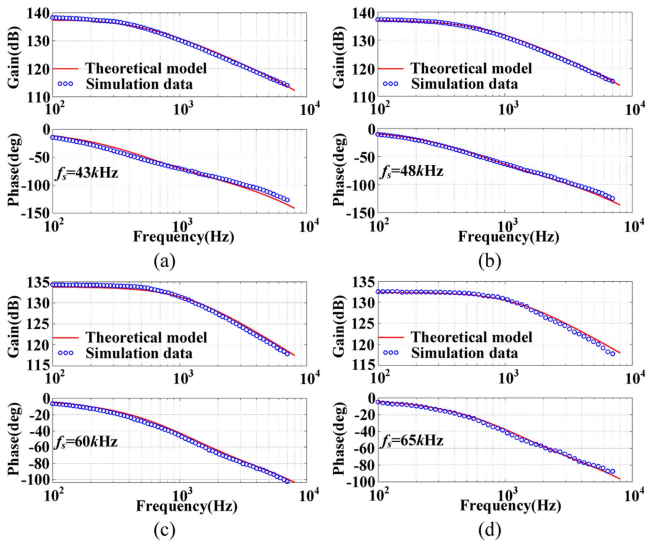

Fig. 13. Simulation results and theoretical model from the control time to the output voltage under TSC. (a) $f_s = 43$ kHz. (b) $f_s = 48$kHz. (c) $f_s = 60$ kHz. (d) $f_s = 65$ kHz.

bode plot is less than 180° in the high-frequency range, which limits the bandwidth of the system.

Similarly, the small signal model of the *LLC* resonant converter under TSC is simulated by the same method. The theoretical model and simulation results of the bode diagram from the control time to the output voltage are shown in Fig. 13. The theoretical model also agrees with the simulation results under $f_s > f_r$ and $f_s < f_r$, which verifies the validity of the theoretical model under TSC.

By comparing the small signal models of the *LLC* resonant converter under PFM and TSC, the bode diagram of the *LLC* under TSC is close to the first-order characteristic. Therefore, it is easier to achieve higher bandwidth and high phase margin

TABLE III
DETAILED SPECIFICATIONS

Items	Symbols	Specifications
Core size of the resonant inductor	L_r	PQ32/32
Resonant capacitor	C_r	Polypropylene film capacitor
Core size of the transformer	T_r	PQ40/40
Switches	$S_{1\text{-}4}$	IRFB4110PBF
Diodes	$D_{r1\text{-}4}$	SFA60UP60S
Input filter capacitor	C_{in}	KNSCHA 152EC0326
Output filter capacitor	C_o	Polypropylene film capacitor

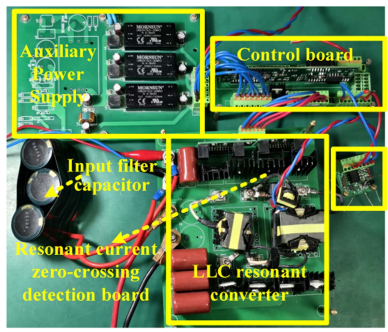

Fig. 14. Experimental prototype.

in closed-loop control, which makes the design of the controller simpler and the dynamic response better.

V. EXPERIEMENTAL VERIFICATION

An experimental prototype of the full-bridge *LLC* resonant converter was built to verify the validity of the small-signal models under PFC and TSC. The circuit parameters are the same as the simulation, and the specifications of the circuit are given in Table III. The PFM and TSC are implemented in a digital signal processor (DSP) TMS320F28035. Fig. 14 shows the experimental prototype, which mainly consists of the *LLC* converter, the control board, the resonant current zero-crossing detection circuit, and the auxiliary power supply. The implementation of TSC in the digital controller is the same as the figure shown in Fig. 7.

A. Experimental Verification of Small Signal Model

To test the bode diagram of the *LLC* converter, small sinusoidal periodic perturbations with different frequencies are added to the switching period. A 50% square waveform with the same frequency and phase as the periodic perturbation is generated by the DSP. The experimental waveforms are shown in Fig. 15, v_{o_AC} is the ac component of the output voltage, and the rising edge of the square waveform indicates 0° of the small sinusoidal perturbation. The gain of the frequency response is equal to the ac amplitude of the output voltage divided by the amplitude of the periodic perturbation. By comparing the phase difference between the square waveform and the ac component of the output voltage, the phase of the frequency response can be obtained.

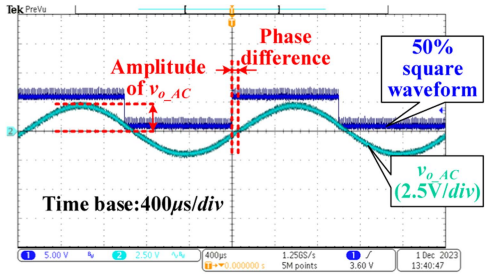

Fig. 15. Experimental waveforms of small-signal verification method.

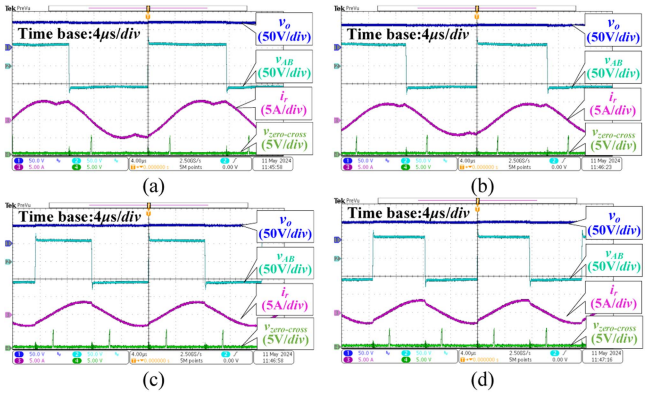

Fig. 16. Waveforms of the steady-state operating points for *LLC* resonant converter. (a) $f_s = 43$ kHz. (b) $f_s = 48$ kHz. (c) $f_s = 60$ kHz. (d) $f_s = 65$ kHz.

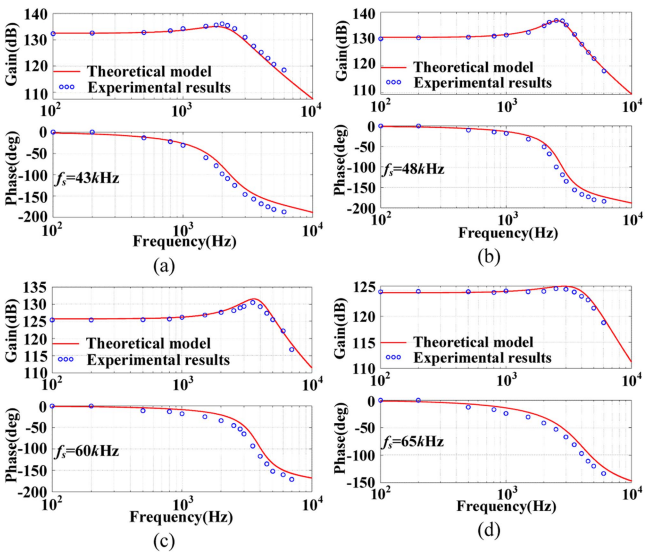

Fig. 17. Experimental results and theoretical model of the bode diagram under PFM. (a) $f_s = 43$ kHz. (b) $f_s = 48$ kHz. (c) $f_s = 60$ kHz. (d) $f_s = 65$ kHz.

Fig. 16 shows the steady-state operating point waveforms of the *LLC* resonant converter at 43, 48, 60, and 65 kHz. The small signal model under PFM is verified at the above steady-state operating points by experiment respectively. The bode diagrams of the *LLC* under PFM are given in Fig. 17. The amplitude gain and phase of the experimental results agree with the theoretical model. The experimental bode diagrams of the *LLC* under TSC are depicted in Fig. 18, and it can be observed that the experimental results match the theoretical model well.

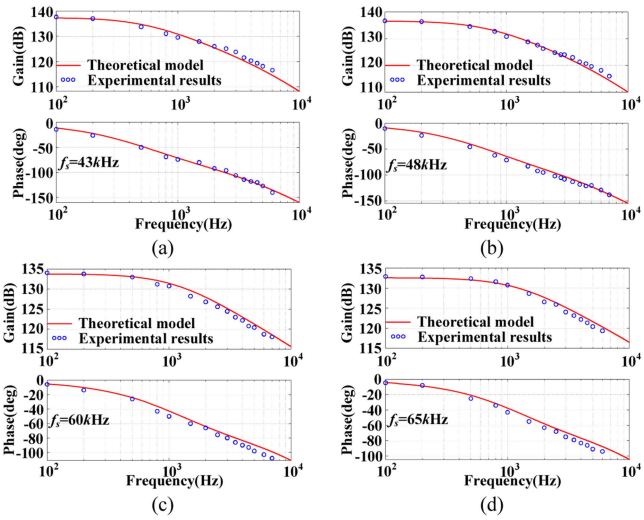

Fig. 18. Experimental results and theoretical model of the bode diagram under TSC. (a) $f_s = 43$ kHz. (b) $f_s = 48$ kHz. (c) $f_s = 60$ kHz. (d) $f_s = 65$ kHz.

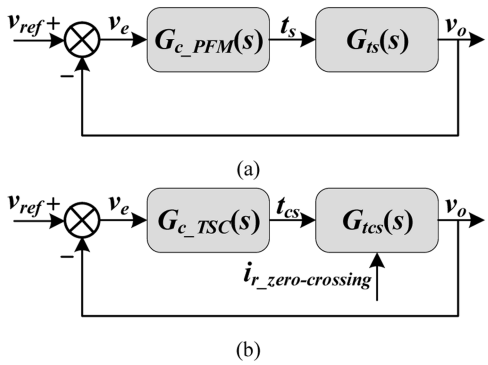

Fig. 19. Block diagram for closed-loop model of the *LLC* converter. (a) Pulse frequency modulation. (b) Time-shift control.

Comparative analysis of the experimental results under PFM and TSC reveals that within the frequency range of 2 to 4 kHz, the small-signal model under PFM exhibits resonance peaks. Furthermore, the positions of these resonance peaks vary with different switching frequencies, thereby posing challenges to the design of closed-loop controllers and the stability of closed-loop systems for PFM. In TSC, resonance peaks are eliminated and the small-signal model presents nearly a first-order frequency response, which possesses a better dynamic response in closed-loop control and facilitates controller design.

B. Design Example of the Closed-Loop Controller

This subsection presents a closed-loop control with 50–70 V input voltage, 60 V output voltage, and 300 W rated load power. To compare the dynamic characteristics of the *LLC* converter under PFM and TSC, proportional-integral (PI) controllers need to be designed based on the proposed small signal model. The block diagram for the closed-loop model is shown in Fig. 19,

TABLE IV
COMPARATIVE ANALYSIS OF SMALL SIGNAL MODELS

	Proposed model	Discrete time model [27]	EDF model [24]	SRF model [22]	Equivalent circuit model [21]	FHA model [17]
Analysis domain	Time domain	Time domain	Frequency domain	Frequency domain	Frequency domain	Frequency domain
Derivation	Moderate	Moderate	Complex	Simple	Simple	Simple
Applicable range	Wide	Wide	Wide	Near the f_r	Near the f_r	Near the f_r
Accuracy	High	High	High	Moderate	Moderate	Low
Extension to TSC	Yes	No	No	No	No	No

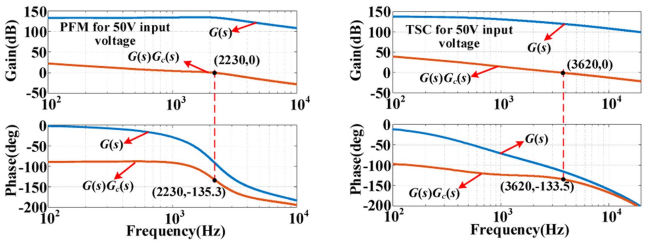

Fig. 20. Bode diagrams of the controller design for 50 V input voltage. (a) PFM. (b) TSC.

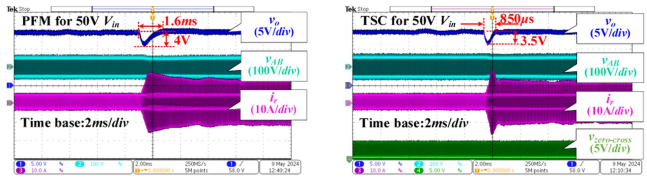

Fig. 21. Dynamic waveforms for 50 V input voltage under the load step change from 50 to 300 W load power. (a) PFM. (b) TSC.

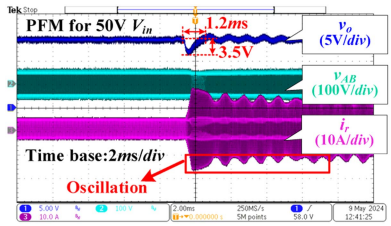

Fig. 22. Oscillatory waveforms of PFM for 50V input voltage under the load step change from 50 to 300 W load power.

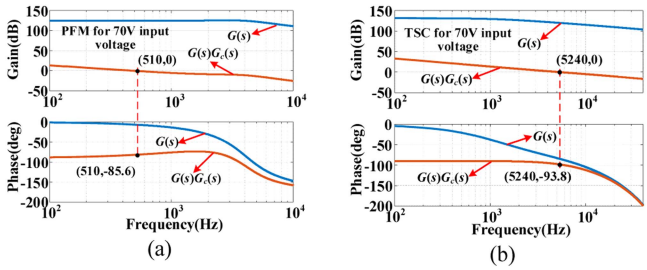

Fig. 23. Bode diagrams of the controller design for 70 V input voltage. (a) Pulse frequency modulation. (b) Time-shift control.

where $G_c(s)$ is the transfer function of the PI controller, and $G(s)$ is the small-signal transfer function of the *LLC* converter from the control variable to the output voltage. For PFM, $G(s)$ is $G_{ts}(s)$. For TSC, $G(s)$ is $G_{tcs}(s)$.

As seen in Fig. 17, it can be observed that the converter operating in boost mode (PO mode) under PFM has a larger phase lag. To ensure system stability throughout the full input voltage range, the parameters of the PI controller need to be designed under this operating condition. Given an output voltage of 60 V and a rated power of 300 W, the design of the PI controller for an input voltage of 50 V is shown in Fig. 20, and the expressions for the controllers under PFM and TSC are expressed in (56) and (57), respectively. It can be seen that the converter under TSC exhibits a higher crossover frequency while ensuring sufficient phase margin, implying better dynamic response

$$G_{c\_PFM}(s) = \frac{1.485 \times 10^{-7}\left(s + 1.194 \times 10^{4}\right)}{s} \tag{56}$$

$$G_{c\_TSC}(s) = \frac{9.372 \times 10^{-7}\left(s + 8.168 \times 10^{3}\right)}{s}. \tag{57}$$

At an input voltage of 50 V, the converter operates in PO mode. The load step experiments from 50 to 300W are depicted in Fig. 21, where the captured output voltage v_o has a bias of 45 V. It is evident that under TSC, the converter exhibits a smaller overshoot and settling time. Moreover, increasing the proportional gain of the PI controller under PFM to enhance dynamic response results in significant oscillation, as depicted in Fig. 22. The dynamic response in Fig. 22 is still lower than that under TSC.

Using the PI controller shown in (56) and (57) for 70 V input voltage, the converter operates in NP mode. The bode diagrams for the PFM and TSC in closed-loop control are illustrated in Fig. 23. It can be observed that the converter exhibits a higer phase margin and the crossover frequency under TSC. However, the crossover frequency decreases under PFM. The load step experiments from 50 to 300 W are shown in Fig. 24. The experimental results demonstrates better dynamic response under TSC, while the dynamic reponse deteriorates under PFM.

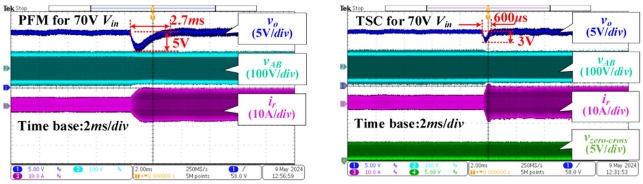

(a) (b)

Fig. 24. Dynamic waveforms for 70 V input voltage under the load step change from 50 to 300 W load power: (a) Pulse frequency modulation. (b) Time-shift control.

C. Comparative Analysis of the Models

The comparison analysis of different methods for the small-signal modeling of *LLC* converters given in Table IV. Although the FHA model, the SRF model, and the equivalent circuit model can provide simple analysis, they only have higher accuracy near the resonant frequency. When the switching frequency deviates from the resonant frequency, their accuracy decreases. The EDF method proposed in [24], which considers all harmonic components, can provide an accurate small-signal model. However, it involves an overly complex derivation process and does not provide specific expressions for transfer functions. The discrete-time model can derive an accurate small-signal model, but these methods are difficult to extend to the derivation of the small-signal model for TSC. The method proposed in this article not only derives the high-precision small-signal model in a wide range of switching frequency based on the time-domain analysis but also facilitates the extension to the derivation of the small-signal model for TSC, which can provide valuable guidance for controller design and contribute to better frequency response.

VI. Conclusion

The article presents a new method to do the small-signal modeling of the *LLC* converter for both PFM and TSC. The previous small-signal models for the PFM are difficult to extend to the TSC, and the analysis of the frequency response for the TSC is based on simulation. In this article, the state trajectory of the *LLC* resonant converter is analyzed, and the equations for calculating the steady-state operating point are obtained based on the time-domain analysis. According to the expressions of the state trajectory, an accurate small-signal model is derived based on the Tylor's expansion, which demonstrates high accuracy in a wide range of switching frequency. Moreover, this method can be extended to the small-signal modeling of TSC. The frequency response between the PFM and TSC is compared. The simulation data and experimental results verify the validity of the theoretical model, which provides valuable guidance for the design of the controller. The closed-loop PI controller is designed based on the small-signal model, and load step experiments demonstrate that the converter exhibits better dynamic response under TSC compared to PFM.

References

[1] M. H. Ahmed, C. Fei, F. C. Lee, and Q. Li, "48-V voltage regulator module with PCB winding matrix transformer for future data centers," *IEEE Trans. Ind. Electron.*, vol. 64, no. 12, pp. 9302–9310, Dec. 2017.

[2] F. Musavi, M. Craciun, D. S. Gautam, and W. Eberle, "Control strategies for wide output voltage range LLC resonant DC–DC converters in battery chargers," *IEEE Trans. Veh. Technol.*, vol. 63, no. 3, pp. 1117–1125, Mar. 2014.

[3] J. Y. Lee, Y. S. Jeong, and B. M. Han, "An isolated DC/DC converter using high-frequency unregulated LLC resonant converter for fuel cell applications," *IEEE Trans. Ind. Electron.*, vol. 58, no. 7, pp. 2926–2934, Jul. 2011.

[4] H.-P. Park and J.-H. Jung, "PWM and PFM hybrid control method for LLC resonant converters in high switching frequency operation," *IEEE Trans. Ind. Electron*, vol. 64, no. 1, pp. 253–263, Jan. 2017.

[5] S. Bai and Y. Bai, "The study of controlling strategy of LLC resonant converter charger," in *Proc. 21st Int. Conf. Elect. Machines Syst.*, 2018, pp. 2230–2233.

[6] S. -W. Kang, H. -J. Kim, and B. -H. Cho, "Adaptive voltage-controlled oscillator for improved dynamic performance in LLC resonant converter," *IEEE Trans. Ind. Applicant.*, vol. 52, no. 2, pp. 1652–1659, Mar./Apr. 2016.

[7] J. Jang, M. Joung, S. Choi, Y. Choi, and B. Choi, "Current mode control for LLC series resonant dc-to-dc converters," in *Proc. Appl. Power Electron. Conf. Expo.*, 2011, pp. 21–27.

[8] J. Jang, P. S. Kumar, D. Kim, and B. Choi, "Average current-mode control for LLC series resonant dc-to-dc converters," in *Proc. Int. Power Electron. Motion Control Conf.*, 2012, pp. 923–930.

[9] "Advanced secondary side LLC resonant converter controller with synchronous rectifier control," 2015. [Online], Available: https://www.onsemi.com/download/data-sheet/pdf/fan7688-d.pdf

[10] Y. -H. Hsieh and F. C. Lee, "Accurate small-signal modeling for charge-controlled LLC resonant converter," in *Proc. IEEE Energy Convers. Congr. Expo.*, 2021, pp. 3052–3059.

[11] Z. Hu, L. Wang, Y.-F. Liu, and P. C. Sen, "Bang-Bang charge control for LLC resonant converters," in *Proc. IEEE Energy Convers. Congr. Expo.*, 2013, pp. 140–146.

[12] "UCC256302 LLC resonant controller with high voltage startup enabling low standby power," 2017. [Online], Available; https://www.ti.com/product/UCC256302?keyMatch=UCC256302

[13] C. Adragna, "Time-shift control of LLC resonant converters," in *Proc. PCIM Eur. Proc.*, May 2010, pp. 661–666.

[14] "Digital combo multi-mode PFC and time-shift LLC resonant controller," 2022. [Online], Available. https://www.st.com/en/power-management/stnrg011.html

[15] C. Adragna, D. Ciambellotti, M. Dell'Oro, and F. Gallenda, "Digital implementation and performance evaluation of a time-shift-controlled LLC resonant half-bridge converter," in *Proc. IEEE Appl. Power Electron. Conf. Expo.*, 2014, pp. 2074–2080.

[16] G. W. Wester and R. D. Middlebrook, "Low-frequency characterization of switched DC-DC converters," *IEEE Trans. Aerosp. Electron. Syst.*, vol. AES-9, no. 3, pp. 376–385, May 1973.

[17] E. X. Yang, F. C. Lee, and M. M. Jovanovic, "Small-signal modeling of series and parallel resonant converters," in *Proc. 7th Annu. Appl. Power Electron. Conf. Expo.*, 1992, pp. 785–792.

[18] C. -H. Chang, C. -A. Cheng, and H. -L. Cheng, "Modeling and design of the LLC resonant converter used as a solar-array simulator," *IEEE J. Emerg. Sel. Topics Power Electron.*, vol. 2, no. 4, pp. 833–841, Dec. 2014.

[19] G. Ghosh, S. Vyapari, and N. R V., "Comparison of modeling approaches for LLC resonant converter based on extended describing function," in *Proc. 11th Int. Conf. Power Electron. ECCE Asia*, 2023, pp. 3327–3332.

[20] C. -H. Chang, E. -C. Chang, C. -A. Cheng, H. -L. Cheng, and S. -C. Lin, "Small signal modeling of LLC resonant converters based on extended describing function," in *Proc. Int. Symp. Comput., Consum. Control*, 2012, pp. 365–368.

[21] S. Tian, F. C. Lee, and Q. Li, "Equivalent circuit modeling of *LLC* resonant converter," *IEEE Trans. Power Electron.*, vol. 35, no. 8, pp. 8833–8845, Aug. 2020.

[22] D. J. Kapupara, "Modeling of LLC converter using synchronous reference frame transformation approach," in *Proc. IEEE Int. Power Renew. Energy Conf.*, 2020, pp. 1–6.

[23] B. Cheng, F. Musavi, and W. G. Dunford, "Novel small signal modeling and control of an LLC resonant converter," in *Proc. IEEE Appl. Power Electron. Conf. Expo.*, 2014, 2014, pp. 2828–2834.

[24] Y. -H. Hsieh and F. C. Lee, "Accurate small-signal model for LLC resonant converters," in *Proc. IEEE Energy Convers. Congr. Expo.*, 2019, pp. 660–665.

[25] X. Fang, H. Hu, Z. J. Shen, and I. Batarseh, "Operation mode analysis and peak gain approximation of the LLC resonant converter," *IEEE Trans. Power Electron.*, vol. 27, no. 4, pp. 1985–1995, Apr. 2012.

[26] X. Fang et al., "Efficiency-oriented optimal design of the LLC resonant converter based on peak gain placement," *IEEE Trans. Power Electron.*, vol. 28, no. 5, pp. 2285–2296, May 2013.
[27] Y. Zhang and X. Ruan, "Discrete-time small-signal modeling of LLC resonant converter considering the nonlinearity of voltage-controlled oscillator," *IEEE Trans. Ind. Electron.*, vol. 71, no. 3, pp. 2416–2428, Mar. 2024.
[28] S. Zhang, Y. Wei, and J. Liu, "A dynamic time-domain based accurate small signal model for LLC converter," in *Proc. IEEE 14th Int. Symp. Power Electron. Distrib. Gener. Syst.*, 2023, pp. 984–989.
[29] W. Feng, F. C. Lee, and P. Mattavelli, "Simplified optimal trajectory control (SOTC) for LLC resonant converters," *IEEE Trans. Power Electron.*, vol. 28, no. 5, pp. 2415–2426, May 2013.

Zhiqiang Guo (Senior Member, IEEE) received the B.S. degree in automation from the Hebei University of Technology, Tianjin, China, in 2008, and the M.S. and Ph.D. degree in electrical engineering from the Beijing Institute of Technology, Beijing, China, in 2010 and 2015, respectively.

He was a Postdoctoral Research Fellow with the Department of Electrical Engineering, Tsinghua University, Beijing, China, from 2015 to 2017. In 2017, he was the Faculty of the School of Automation, Beijing Institute of Technology, Beijing, China, where he is currently an Associate Professor. He has authored more than 40 papers and two books in the field of power electronics. His current research interests include dc–dc converters, distributed generation, and microgrid applications.

Zhijie Huang received the B.S. degree in automation from the Shandong University, Jinan, China, in 2022. He is currently working toward the M.S. degree in control science and engineering with Beijing Institute of Technology, Beijing, China.

His current research interests include control and modeling of the bidirectional dc–dc converters and switching power supply.

Zhongyuan Chen received the B.S. and M.S. degrees in electrical engineering from Beijing Institute of Technology, Beijing, China, in 2009 and 2012, respectively.

In 2012, he was with Beijing Institute of Smart Energy, Beijing, China, where he is currently a Senior Engineer. His current research interests include dc–dc converters, testing and application of Power Semiconductor Devices.